

Quasi-Steady Magnetoplasmadynamic Thruster Measured Performance Database *

E.Y. Choueiri[†] and J.K. Ziemer[‡]
Electric Propulsion and Plasma Dynamics Laboratory (EPPDyL)
MAE Dept.
Princeton University
Princeton, New Jersey 08544

AIAA-98-3472[§]

Abstract

The performance of a coaxial, gas-fed, self-field, quasi-steady pulsed magnetoplasmadynamic thruster (MPDT) was measured using a swinging gate thrust stand equipped with a laser interferometer and an RF proximeter. Careful calibration of the thrust stand, and other diagnostics insured that the measurement errors, barring the effects of fluctuations in the discharge voltage, are well below 2%. The measurements were carried for various mass flow rates, ranging between .5 and 6 g/s and for four propellant gases: argon, xenon, hydrogen and deuterium. The data set can be interpreted to describe both the performance of 1) steady-state high-power (multimegawatt) MPDTs and 2) quasi-steady *pulsed* MPDTs that can operate at arbitrarily low spacecraft bus power. The results were curve-fit and compiled into a performance database that is intended as a data source for system or mission analysis as well as for the validation of analytical and numerical models of the MPDT.

1 Introduction

1.1 Status of MPDT Technology

Quasi-steady pulsed operation of self-field magnetoplasmadynamic thrusters (MPDTs) was originally

intended[1, 2] as a means of simulating high power (multimegawatt) steady-state thrusters in the laboratory. The need to operate at high instantaneous power stems from the early[3] recognition that MPDTs operate more efficiently with increasing power¹. Two facts eventually became clear by the late eighties. First, the prospects of MW-level power in space had considerably receded with the continuous lack of evolution in space nuclear power programs. Second, the regime in which MPDTs start to become efficient is also that in which cathode erosion rates tend to be prohibitive. In the past few years, two approaches around these two obstacles have been adopted.

The first approach, followed presently in the US and Russia, is the revival of interest[5] in alkali metal (specifically lithium) MPDTs with multi-channel cathodes. These steady-state thrusters, sometimes called Lorentz Force Accelerators (LFAs) to differentiate them from gas-fed solid cathode MPDTs, have substantially low cathode erosion rates[6, 7] with the added benefit of better performance attributed to the low ionization losses of lithium propellant. Although acceptable lifetimes are now well within reach and 50% efficiencies are accessible at powers as low as 100 kW[8, 5] (using applied magnetic fields²), there are still no source power sources at these levels. Consequently the Lithium LFA is presently of little interest to commercial satellites and more appropriate for more futuristic planetary exploration missions being

*Research supported by NASA-JPL's program on advanced propulsion.

[†]Chief Scientist at EPPDyL. Assistant Professor, Applied Physics Group, MAE Dept. and Associated Faculty at the Dept. of Astrophysical Sciences. Senior Member AIAA.

[‡]Graduate Student, Research Assistant. Member AIAA.

[§]Presented at the 34th AIAA Joint Propulsion Conference, Cleveland, OH, July 13-16, 1998.

¹A major reason for that dependency is the diminution of the anode power loss fraction with increasing power[4].

²Applied magnetic fields are typically only needed for efficient operation below 200 kW.

studied at NASA[5].

The second approach, followed presently in Japan and Europe, is more suited for near-term applications. It considers the pulsed quasi-steady MPDT not anymore as a device for laboratory simulation of steady-state high power thrusters, but as a *low power* propulsion option in itself. In this incarnation, the quasi-steady pulsing (typically a few hundred μs) allows operation at arbitrarily low bus power levels and may be advantageous for some near-term missions[9]. Although cold cathode erosion still limits the spectrum of missions due to the limit on the total impulse that a single thruster may deliver, schemes for active cathode heating[10] may soon expand this spectrum. Advances in energy storage technologies and valve technologies are essential to improve the prospects of pulsed MPDTs[11]. Last year witnessed the first flight test of a 1-kW class gas-fed self-field quasi-steady MPDT on the Japanese SFU spacecraft[12].

1.2 Motivation for Performance Characterization

System and mission studies in which quasi-steady gas-fed MPDTs are considered or compared to other options need to rely on accurate performance databases in which the key operation parameters are varied parameterically. Similarly, theoretical models and numerical simulations can benefit from such experimental databases for validation and refinement.

Experimental characterization of the performance of quasi-steady gas-fed, self-field MPDTs have been published by Japanese workers in Refs. [13] for H_2 , [14] for NH_3 , CH_4 , Ne , O_2 , [15] for He and [16] for Ar , He and NH_3 using various thruster geometries. Similar studies were published by European workers[17].

A compilation of some of the highest thrust efficiencies measured in the past with gas-fed quasi-steady megawatt-level coaxial self-field MPDTs is shown in Table 1.

In the US, the Princeton full-scale benchmark MPDT has been the subject of numerous detailed studies from 1969 to 1994[20] resulting in the most extensive characterization (species, densities, temperatures, oscillations, erosion, discharge symmetry, electrode power deposition, etc.) of a single MPDT geometry. In contrast, measured performance characterization of that same thruster is limited to a single³

³A more limited thrust characterization of that thruster was also made in Refs. [19] and [21]

database for argon and nitrogen published by Burton et. al.[18] in 1983. The main goal of this paper is to update and extend this database to include low atomic mass propellant such as hydrogen and deuterium and high atomic mass propellant such xenon. Xenon is also interesting for system and mission analysis where integration with xenon ion or hall thrusters may be an option.

This paper describes the measurements and the resulting performance database avoiding any speculation, theoretical or otherwise, on the nature of the dependencies. Such theoretical interpretations are published elsewhere[22].

2 Apparatus

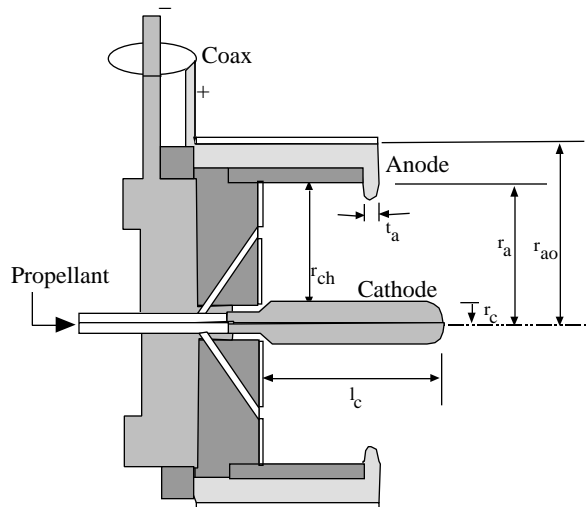


Figure 1: Schematic of the Princeton full-scale benchmark thruster used for the present study. The dimensions are $r_c = 0.95$ cm, $r_a = 5.1$ cm, $r_{ao} = 9.3$ cm, $r_{ch} = 6.4$ cm, $t_a = 0.95$ cm and $l_c = 10$ cm.

The MPDT used for the experiments is the so-called Princeton full-scale benchmark thruster (FSBT) shown schematically in Fig. (1) where the dimensions are also given. It is the same one used by Burton et. al[18] and is described in more detailed in that paper. In brief, the cathode is made of thoriated tungsten, the anode is an annular aluminum disk, the backplate insulator is boron nitride and the side insulator is a Pyrex tube. The exterior is insulated with a nylon sleeve. Propellant is injected through a

	H ₂	N ₂	NH ₃	CH ₄	Ar	Ne	He	O ₂
η (%)	55	38	35	33	30	20	20	18
I_s (s)	10000	4000	5700	6000	2300	4000	2000	2500
Reference	[13]	[18]	[14]	[14]	[19]	[14]	[15]	[14]

Table 1: Some of the highest measured efficiencies for the coaxial self-field MPDT with various gaseous propellants.

solenoid valve feeding a choked multiple orifice which splits the flow into a portion (54%) going an annulus around the cathode base and the other (46%) going through a ring of 12 holes in the backplate located at a radius of 3.8 cm.

The mass flow rate calibration consisted of calibrating the gas flow rate through the choked orifice injection system as a function of the pressure located just upstream of the orifices. This was done by flowing gas, for various mass pulse lengths and plenum pressures into an enclosure of known volume and monitoring the increase in the pressure. The calibration of the mass injection system used in this study is described in details in the appendix of ref. [21].

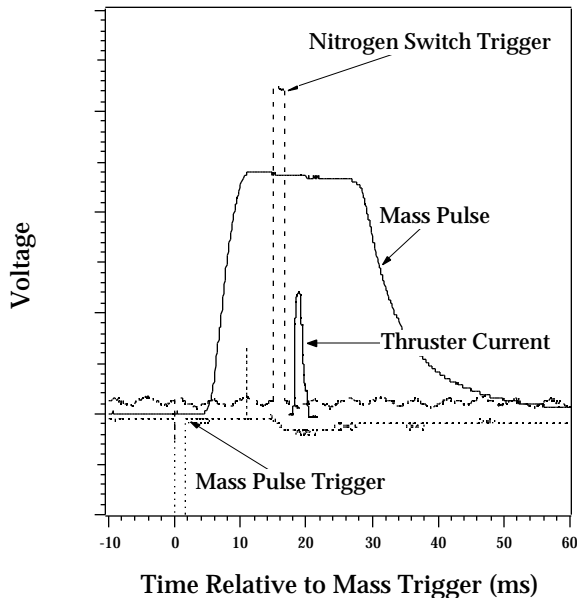


Figure 2: Timing of mass pulse and thruster triggers.

The triggers to the mass pulse and the nitrogen switch controlling the discharge circuit are shown in Fig. (2) along with the waveforms for the mass pulse

and thruster current. Sample thruster current and voltage waveforms are shown on an expanded scale in Fig. (3). As seen in that figure, the discharge current is a quasi-steady flat top multi-kA pulse of about 1 ms. The voltage is on the order of 100 V and acquires oscillations, called voltage “hash” for operation above a certain current. The voltage hash is the major source of the error bars in the database.

The current waveform is supplied by a 20-station 12.8 mfarad L-C pulse forming network (PFN) with an energy storage capability of 120 kJ and can produce rectangular current pulses ranging from .5 to 2 msecs and current levels up to 50 kA. All experiments reported here were done at the 1 ms pulse length setting. The 40 m Ω PFN is matched to the 10 m Ω thruster impedance with a series 30 m Ω resistor. A nitrogen gas switch is used to trigger the discharge as shown in Fig. (2). The discharge current is measured with a current transformer and the voltage with a 1000:1 Tektronix probe.

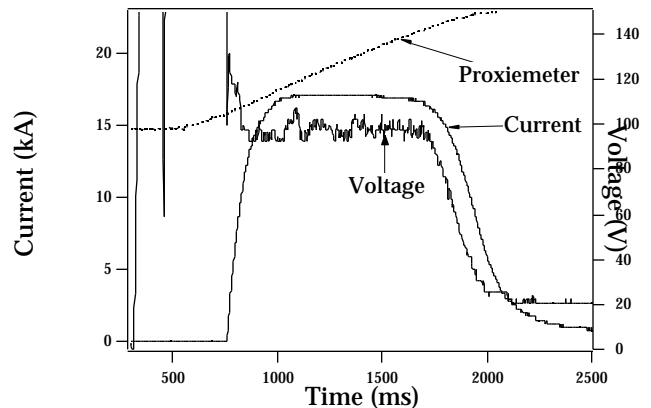


Figure 3: Sample waveforms for thruster current and voltage and thrust stand proximeter response.

The vacuum vessel is a 2 m diameter, 5 m long fiberglass tank with eight optical access ports. A vac-

uum level on the order of 10^{-5} torr, is maintained by a set of two 1.3 m (48-inch) CVC diffusion pumps each with a pumping capability of 120,000 l/s. The diffusion pumps are backed by a roots blower (1340 cfm) and two mechanical pumps (300 cfm).

2.1 Thrust Stand

The thruster assembly weighs about 20 kg and is mounted on a “swinging gate” thrust stand as shown schematically in Fig. (4). The thrust arm is mounted with two flexural pivots. They are series 6016 Bendix Free-Flex Pivots each with a torsional spring constant of 0.73 N-m/rad. The vertical axis of rotation of the arm can be adjusted to incorporate the force of gravity. The force of gravity can be added or subtracted from the restoring force of the flexural pivots to influence the natural period of the arm. Typical natural periods of the arm are 1-10 seconds. The thrust stand arm is fully described in Ref. [18] and is a modified version of a microthrust stand built by Fairchild Republic[23]. To reduce random mechanical perturbations to the thrust stand system, the entire thrust stand table was mechanically isolated from the tank. This was done by resting the entire structure on rubber supports.

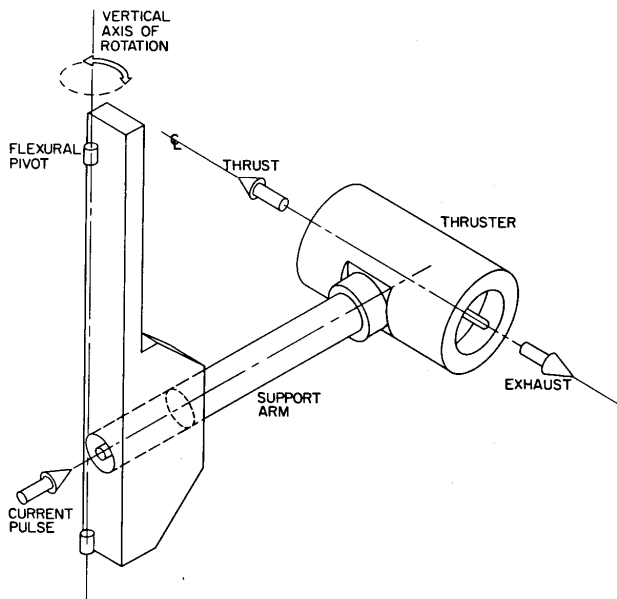


Figure 4: Schematic of “swinging gate” thrust stand.

2.2 Thrust Arm Displacement Measurement

The thruster position is measured simultaneously with an RF proximeter and an optical interferometric proximeter system (IPS). The two measurements were always in agreement and the IPS was relied on for small impulses such as during the cold gas shots.

The RF proximeter is a highly linear 8V/mm Bently-Nevada position transducer. The transducer is located 0.61 m from the hinge axis and measures the displacement of a 4140 allow steel target mounted on the thruster.

The laser-based IPS was described in detail in a recent publication[24]. It is mounted on an optical table attached to an access window behind the thruster as shown in Fig. 5. Light emitted from the laser source is split into two beams at the beam splitter. At the end of each path is a corner cube. The two beams are reflected back to the beam splitter and passed through a lens to the diode sensors. The diode sensor output signals are recorded on a computer. Multiple fringes are facilitated by slightly offsetting the two beams at the diode sensors. When the path lengths traversed by the two beams differ by a non-integer multiple of the wavelength of the laser light (λ) there is a phase angle difference (ϕ) between them when they are reunited. Superposition of these two waves yields constructive or destructive interference. Analysis of the electronically recorded interference pattern yields a position measurement with a 10 nm accuracy[24].

One corner cube is attached to the thrust stand table and the other to the thruster. A 1 mW Helium-Neon laser ($\lambda=632.8$ nm) was used as a light source in the interferometer. Both the beam splitter and the right angle prism were mounted on two adjoined aluminum blocks with separate pitch angle adjustment. Also the beam splitter and right angle prism can each slide sideways to match the horizontal separation of the corner cubes. Both of these adjustments are made until both beams are nearly coincident at the adjustable mirror. The mirror is then used to direct the beams to the diode sensors. Between the mirror and the diodes are a lens and a filter. The lens is a cylindrical lens of focal length 1 cm. Finally there is a 3 nm bandwidth filter at wavelength 632.8 nm. This prevents virtually all of the stray light from the surroundings from reaching the diode sensors, including light from the plasma discharge. The diode sensors are FDS100 Silicon Photodiodes from Thorlabs Inc. They have a rise time of 10 ns, an active area of 13.7 mm², and a spectral response of 350-1100 nm.

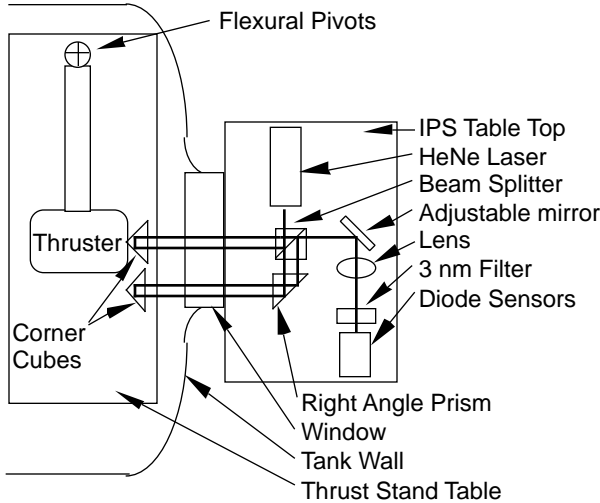


Figure 5: Layout of the interferometric proximeter system (IPS).

2.3 Calibration Pendulum

Deducing the impulse from the position measurement requires the knowledge of the effective mass, m_{eff} of the the thruster-thrust arm assembly. This was done using a calibration pendulum. The calibration impulse was delivered by a 30-cm-long 0.5-kg-steel rod that was used as a pendulum. The rod pivots on a teflon pin which was fixed to an aluminum stand. This stand was mounted inside of the vacuum tank in front of the thruster and struck the thruster while the vacuum tank was exposed to atmosphere. An electromagnet was also mounted on the pendulum stand so that the pendulum could be cocked and then released remotely. The force transducer used was a model 208A02 Force Transducer from Piezotronics and was attached to the end of the pendulum which struck the thruster. The operating range is from 0-400 N. A quantification of the calibration error is given in ref. [24]. The calibration yielded a value of 15.71 ± 0.27 kg for m_{eff} .

2.4 Thrust Measurement Method

If the motion of the thrust thruster during a pulse is characterized by x , and the effective natural frequency, damping constant, and mass are $\omega_{n,eff}$, ζ_{eff} , and m_{eff} respectively, the applied impulse bit (I_{bit})

will force the response[24]

$$x(t) = e^{-\zeta_{eff}\omega_{n,eff}t} \frac{I_{bit}/m_{eff}}{\omega_{n,eff}\sqrt{1-\zeta^2}} \sin\left(\sqrt{1-\zeta^2}\omega_{n,eff}t\right). \quad (1)$$

The duration of the impulse must be much less than the natural period of the thrust stand for Eq. 1 to be valid. In many such cases, measurements can be made on time scales where the effects of the spring and damper are negligible. In the absence of a spring and damper, this model leads to the simple momentum equation,

$$I_{bit} = m_{eff}\Delta\dot{x}, \quad (2)$$

where $\Delta\dot{x}$ is the change in velocity of the observation point from before to after the impulse. Likewise, for a free body, Newton's equation,

$$\ddot{x} = T/m_{eff}, \quad (3)$$

governs the dynamics where \ddot{x} is the acceleration of the observation point and T is the instantaneous thrust. In order to compute I_{bit} or T , a calibration constant, the effective mass (m_{eff}), for the thrust stand must be determined as discussed in Section 2.3 above.

Both the IPS and the RF proximeter give a measure of $\Delta\dot{x}$. For example a sample experiment yields a slope change of 5.79 mm/s. From Eq. 2 and $m_{eff} = 15.71 \pm 0.27$ kg, the delivered impulse is $I_{bit} = 15.71 \text{ kg} \times 5.79 \text{ mm/s} = 0.091 \pm 0.0016 \text{ N}\cdot\text{s}$. A sample position history from the proximeter is shown in Fig. (3).

3 Data Reduction Algorithm

The procedure followed to acquire and reduce the data is as follows.

1. For a given mass flow rate, a series of cold gas experiments were done during which the position of the thrust arm and the mass pulse were both recorded digitally.
 - (a) The mass pulse was recorded with a pressure transducer in the plenum and, as shown in Fig. (3), lasts for about 40 ms. The average value of the mass pulse plateau during the 8 ms immediately preceding the discharge (in order to avoid EMI contaminated signals) was averaged. The value of this averaged plateau, in volts, is $\langle V_m \rangle$.

An effective time, Δt_m for the mass pulse was obtained from

$$\Delta t_m = \frac{\int V_m(t) dt}{\langle V_m \rangle} \quad (4)$$

where $V_m(t)$ is the mass pulse waveform (in Volts) shown in Fig. (3).

- (b) The mass bit m_b is then calculated from

$$m_b = \dot{m} \Delta t_m \quad (5)$$

- (c) A line fit was made to a 50 ms portion of the recorded position-vs-time signal (of either the IPS or the RF proximeter) starting at a time equal to $\Delta t_m + 5ms$ from the time the mass pulse was triggered. (The data fit takes into account the sinusoidal curvature of the response described by Eq. (1) using a previously determined natural frequency of the thrust arm). This yields $\Delta \dot{x}$.

- (d) The cold gas impulse bit is then calculated from

$$I_{cgb} = m_{eff} \Delta \dot{x}. \quad (6)$$

- (e) The cold gas exhaust velocity u_{cge} is then calculated from $u_{cge} = I_{cgb}/m_b$.

2. The thruster is then fired at that mass flow rate and the waveforms for discharge current, voltage and thruster position are recorded as in the sample shown in Fig. (3).

- (a) A plateau value for the current pulse is obtained by averaging a 200 μs portion of the data taken 700 μs after breakdown. This delay is to insure that the averaging is done in the quasi-steady portion of the discharge. As we did for the cold gas case, this average value of the current plateau $\langle J \rangle$ is then used to obtain an effective “hot” pulse duration Δt_h from the following integral

$$\Delta t_h = \frac{\int J(t) dt}{\langle J \rangle}. \quad (7)$$

- (b) The thruster position history (from the IPS or the proximeter) is analyzed the same way as was done in 1.c above for the cold gas case. This yields the “hot” impulse bit I_{hb} .

- (c) The final impulse bit is calculated from the following expression

$$I_b = I_{hb} - (\Delta t_m - \Delta t_h) \dot{m} u_{cge} \quad (8)$$

which subtracts the impulse due to the cold gas but leaves in the albeit small contribution of the cold gas, *during* the discharge.

3. The voltage “hash” δV is calculated as the standard deviation of the average of a portion of the voltage waveform that corresponds to the portion of the current waveform considered above.

4. The following expressions are then used to evaluate the performance parameters

$$\text{Quasi-steady Thrust: } T = \frac{I_b}{\Delta t_h} \quad (9)$$

$$\text{Specific Impulse: } I_{sp} = T/(\dot{m} g_0) \quad (10)$$

$$\text{Input Power: } P = VJ \quad (11)$$

$$\text{Discharge Energy: } E = \int P dt \quad (12)$$

$$\text{Thrust Efficiency: } \eta_T = \frac{T^2}{2\dot{m}P} \quad (13)$$

$$\text{Impulsive Efficiency: } \eta_I = \frac{I_b^2}{2m_b E} \quad (14)$$

5. The performance database is compiled by repeating the above procedures after varying the discharge current, the mass flow rate or the type of propellant.

4 Final Performance Database and Conclusions

Following the procedures outlined above, a performance database for argon at $\dot{m} = 1, 3$ and 6 g/s, xenon at 3 and 6 g/s, hydrogen at .5 and 1 g/s and Deuterium at 1 g/s were obtained. The data are shown in Figs. 6 to 11. For each gas, a series of four scatter plots including error bars were produced for the following dependencies $T - J$, $V - J$, $\eta_T - I_{sp}$ and $\eta_I - E$.

Fourth order polynomial curve fits were carried for each of the data sets and four line plots corresponding to each of the four scatter plots were produced. In order to keep the line plots clear, the error bars were not added. The error bars can be easily seen in the corresponding scatter plots which retain the same scale as the line plots. In order to facilitate the use of this database by other studies, the coefficients for the curve fits are compiled in Table 2.

The major source for the error bars is the voltage hash which can easily exceed 10% above a certain

critical current. The second major source of the error bars is the scatter in the data taken at the same conditions. The repeatability of the thruster also suffers with increasing current. All other source errors do not contribute more than 2% to the error bars.

Although there has been many studies and much speculation on the level of erosion associated with a particular level of voltage hash, we refrain from speculating, in this purely experimental paper, on the extent to which the high-current portion database is affected by not taking into account the eroded mass. While there are some empirical indications[25, 26, 27] that exceeding 10% voltage hash can lead to significant mass addition through erosion, it must be warned that these thresholds were formulated for operation with argon only and should not, *a priori* be extended to operation with other gases.

References

- [1] D.E.T.F. Ashby, L/ Liebing, A.V. Larson, and T.J. Gooding. Quasi-steady-state plasma acceleration. *AIAA Journal*, 4(5):831–835, 1966.
- [2] K.E. Clark and R.G. Jahn. Quasi-steady plasma acceleration. *AIAA Journal*, 8:216–220, 1970.
- [3] V.M. Nerheim and A.J. Kelly. A critical review of the magnetoplasmadynamic (MPD) thruster for space applications. Technical Report 32-1196, NASA-JPL, JPL, CIT, Pasadena, CA, USA, 1968.
- [4] A.J. Saber. *Anode Power in a Quasi-Steady MPD Thruster*. PhD thesis, Princeton University, Princeton, NJ, USA, 1974.
- [5] S. Leifer. Overview of nasa’s advanced propulsion activities. In *34th Joint Propulsion Conference*, Cleveland, OH, USA, 1998. AIAA-98-3183.
- [6] V.P. Ageyev and V.G. Ostrovsky. High-current stationary plasma accelerator of high power. In *23rd International Electric Propulsion Conference*, Seattle, WA, USA, 1993. IEPC-93-117.
- [7] J.E. Polk and T.J. Pivrotto. Alkali metal propellants for MPD thrusters. In *AIAA/NASA/OAI Conf. on Advanced SEI Technologies*, Cleveland, Ohio, 1991. AIAA-91-3572.
- [8] V. Kim, V. Tikhonov, and S. Semenikhin. Fourth quarterly (final) report to nasa-jpl: 100-150 kw lithium thruster research. Technical Report Contract NASW-4851, RIAME, MAI, Moscow, Russia, April 1997.
- [9] E.Y. Choueiri, A.J. Kelly, and R.G. Jahn. Mass savings domain of plasma propulsion for LEO to GEO transfer. *Journal of Spacecraft and Rockets*, 30(6):749–754, 1993.
- [10] F. Paganucci, P. Rosssetti, and M. Anderenucci. Optimization of the cathode heating technique in a pulsed mpd thruster. In *34th Joint Propulsion Conference*, Cleveland, OH, USA, 1998. AIAA-98-3471.
- [11] R.M. Myers. Electromagnetic propulsion for spacecraft. 1993. AIAA-93-1086.
- [12] K. Toki, Y. Shimuzu, and K. Kuriki. Electric propulsion experiment (EPEX) of a repetitively pulsed MPD thruster system onboard Space Flyer Unit (SFU). In *25th International Electric Propulsion Conference*, Cleveland, OH, USA, 1997. IEPC-97-120.
- [13] H. Tahara, K. Kagaya, and T. Yoshikawa. Hybrid MPD thruster with axial and cusp magnetic fields. In *20th International Electric Propulsion Conference*, Garmisch-Partenkirchen, W. Germany, 1988. AIAA-88-058.
- [14] K. Uematsu, S. Morimoto, and K. Kuriki. MPD thruster performance with various propellants. *Journal of Spacecraft and Rockets*, 22(4):412–416, 1985.
- [15] T. Yoshikawa, Y. Kagaya, and K. Kuriki. Thrust and efficiency of the K-III MPD thruster. *Journal of Spacecraft and Rockets*, 21(5):481–487, 1984.
- [16] T. Yoshikawa, Y. Kagaya, Y. yokoi, and H. Tahara. Performance characteristics of quasi-steady mpd thrusters. In *17th International Electric Propulsion Conference*, Tokyo, Japan, 1984. IEPC-84-58.
- [17] F. Paganucci and M. Anderenucci. Mpd thruster performance using pure gases and mixtures as propellant. In *31st Joint Propulsion Conference*, San Diego, CA, USA, 1995. AIAA-95-2675.
- [18] R.L. Burton, K.E. Clark, and R.G. Jahn. Measured performance of a multi-megawatt MPD thruster. *Journal of Spacecraft and Rockets*, 20(3):299–304, 1983.

- [19] M. Wolff, A.J. Kelly, and R.G. Jahn. A high performance magnetoplasmadynamic thruster. In *17th International Electric Propulsion Conference*, Tokyo, Japan, 1984. IEPC-84-32.
- [20] K.D. Diamant, E.Y. Choueiri, and R.G. Jahn. The role of spot mode transition in the anode fall of pulsed MPD thrusters. In *24th International Electric Propulsion Conference*, Moscow, Russia, 1995. IEPC-95-234.
- [21] J.H. Gilland. The effect of geometrical scale upon MPD thruster behavior. Master's thesis, Princeton University, Princeton, NJ, USA, 1988.
- [22] E.Y. Choueiri. The scaling of thrust in self-field MPD thrusters. Accepted for Publication on 6/1/98. To Appear in the September 98 issue of the *Journal of Propulsion and Power*. 1998.
- [23] Operating instructions for plasma engine microthruster stand. Technical Report RAC 2392-1, PCD-TR-65-1, Republic Aviation Corporation, January 1965.
- [24] E.A. Cubbin, J. Ziemer, E.Y. Choueiri, and R.G. Jahn. Laser interferometric measurements of impulsive thrust. *Review of Scientific Instruments*, 68(6):2339–2346, 1997.
- [25] L.K. Rudolph, R.G. Jahn, K.E. Clark, and W.F. von Jaskowsky. Onset phenomena in self-field MPD arcjets. In *13th International Electric Propulsion Conference*, San Diego, CA, 1980. AIAA-78-653.
- [26] R. A. Rowe. Ablation of an MPD thruster. Master's thesis, Princeton University, Princeton, NJ, USA, 1981.
- [27] D.D. Ho. Erosion studies in an MPD thruster. Master's thesis, Princeton University, Princeton, NJ, USA, 1981.

		\dot{m}	a_1	a_2	a_3	a_4	a_5
Ar	T vs J	1	377.98	-0.18079	3.1921e-05	-2.4151e-09	6.7129e-14
		3	750.21	-0.20133	2.0341e-05	-8.8935e-10	1.4599e-14
		6	273.09	-0.057856	4.6962e-06	-1.5357e-10	1.98e-15
	V vs J	1	3225.4	-1.5769	0.0002855	-2.2072e-08	6.2345e-13
		3	2494.3	-0.63077	6.1034e-05	-2.6138e-09	4.3146e-14
		6	-1412	0.38213	-3.6094e-05	1.4756e-09	-2.155e-14
	η_T vs I_{sp}	1	0.13432	-0.00022441	2.3114e-07	-8.4278e-11	1.0756e-14
		3	-0.36688	0.00098812	-6.5927e-07	1.9143e-10	-2.0134e-14
		6	0.005163	0.00011413	1.5326e-07	-1.5329e-10	3.812e-14
η_I vs E	1	0.11766	-0.00020402	2.5809e-07	-1.093e-10	1.5592e-14	
	3	-0.037394	0.00022161	-8.0438e-08	1.2476e-11	-6.799e-16	
	6	0.095522	-0.00012457	1.505e-07	-4.55e-11	4.3276e-15	
Xe	T vs J	3	-731.65	0.26801	-3.5734e-05	2.0942e-09	-4.4838e-14
		6	-133.15	0.046925	-5.3777e-06	2.6879e-10	-4.5162e-15
	V vs J	3	-6137.2	2.3141	-0.0003155	1.8667e-08	-4.0069e-13
		6	323.86	-0.11658	1.7642e-05	-1.0877e-09	2.4557e-14
	η_T vs I_{sp}	3	-0.038003	0.0002198	-9.5391e-08	-2.2799e-11	1.6098e-14
		6	0.033353	-1.2505e-05	2.0121e-07	-1.4834e-10	2.5677e-14
	η_I vs E	3	-0.048114	0.0001767	-8.5315e-08	1.8298e-11	-1.4336e-15
		6	0.038654	-1.7625e-05	3.892e-08	-1.062e-11	8.2645e-16
	H ₂	T vs J	.5	-33.736	0.012505	-1.0358e-06	4.4643e-11
1			-53.66	0.021356	-2.2907e-06	1.2143e-10	-2.0681e-15
V vs J		.5	498.63	-0.15534	2.8127e-05	-1.8256e-09	4.1344e-14
		1	-57.968	0.077804	-6.4875e-06	3.2688e-10	-5.906e-15
η_T vs I_{sp}		.5	-0.11854	0.00013362	-2.0091e-08	1.5514e-12	-4.0884e-17
		1	-0.027978	9.6812e-05	-1.8296e-08	2.079e-12	-7.6783e-17
η_I vs E		.5	-0.1579	0.00024051	-5.4362e-08	5.5818e-12	-1.9217e-16
		1	-0.04706	0.00011432	-2.4302e-08	2.4652e-12	-7.9769e-17
D ₂		T vs J	1	-9.0614	0.0036086	8.8895e-09	-4.6713e-12
	V vs J	1	42.9	0.0154	1.94e-06	1.02e-10	1.92e-15
	η_T vs I_{sp}	1	-0.0032142	7.0845e-05	-8.2522e-09	9.3289e-13	-3.4625e-17
	η_I vs E	1	-0.011218	9.3084e-05	-1.7907e-08	2.154e-12	-8.2666e-17

Table 2: Coefficients for fourth order polynomial curve fits of the measured performance database. The curve fits are only valid for the range of parameters shown in the corresponding plot.

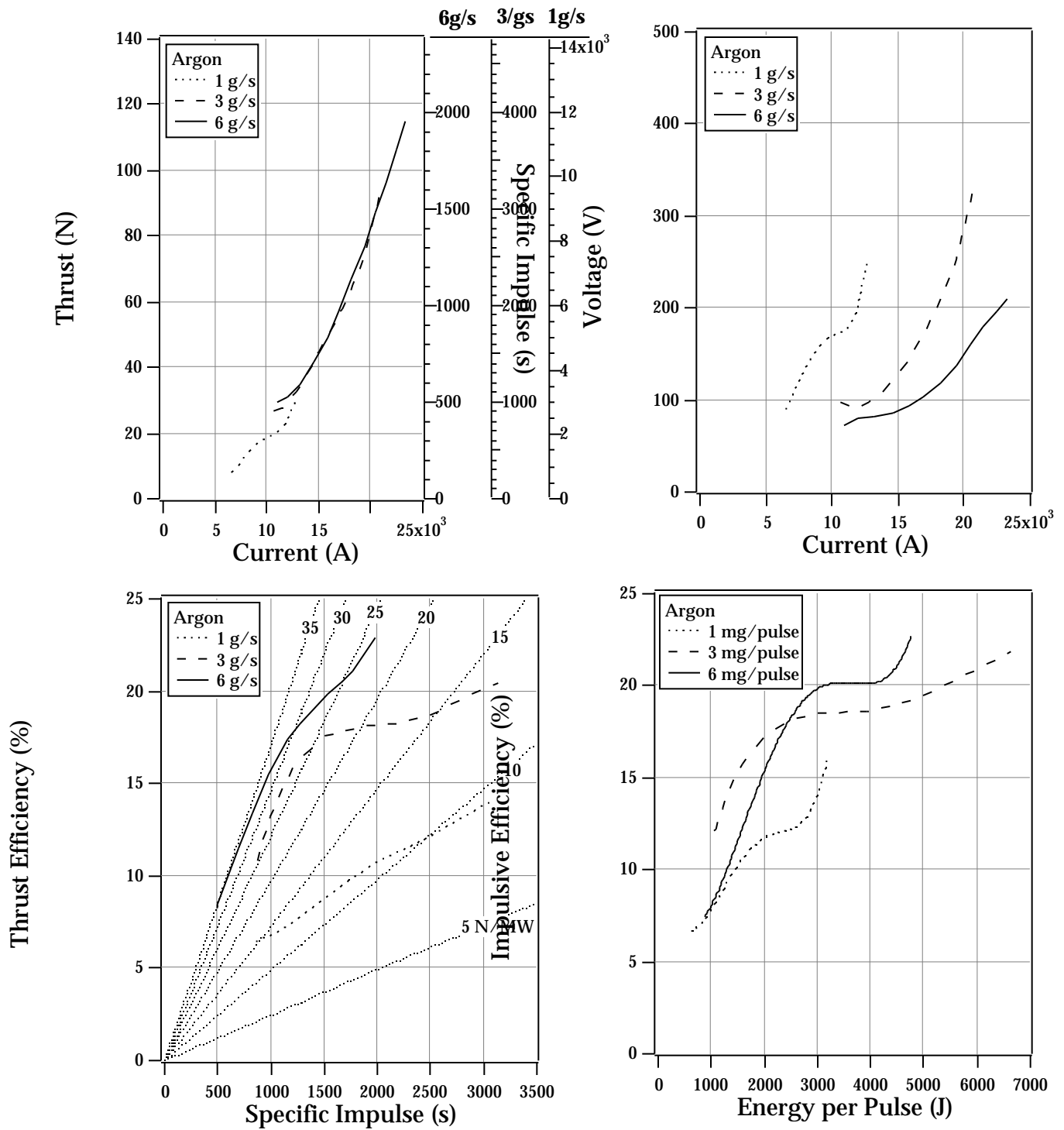


Figure 6: Performance Database for Argon. The corresponding error bars can be obtained from the scatter plots in the next figure.

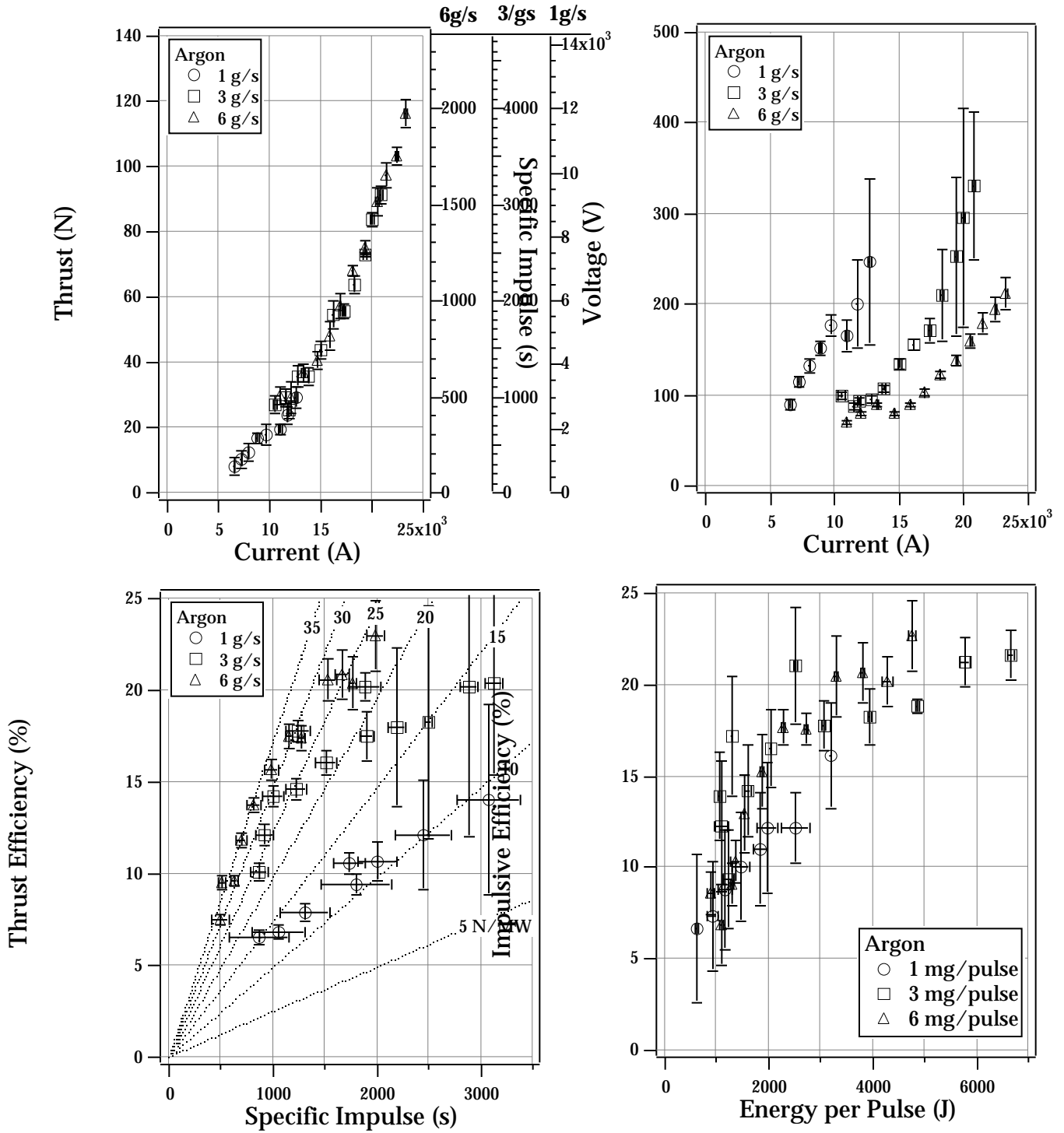


Figure 7: Performance Database for Argon.

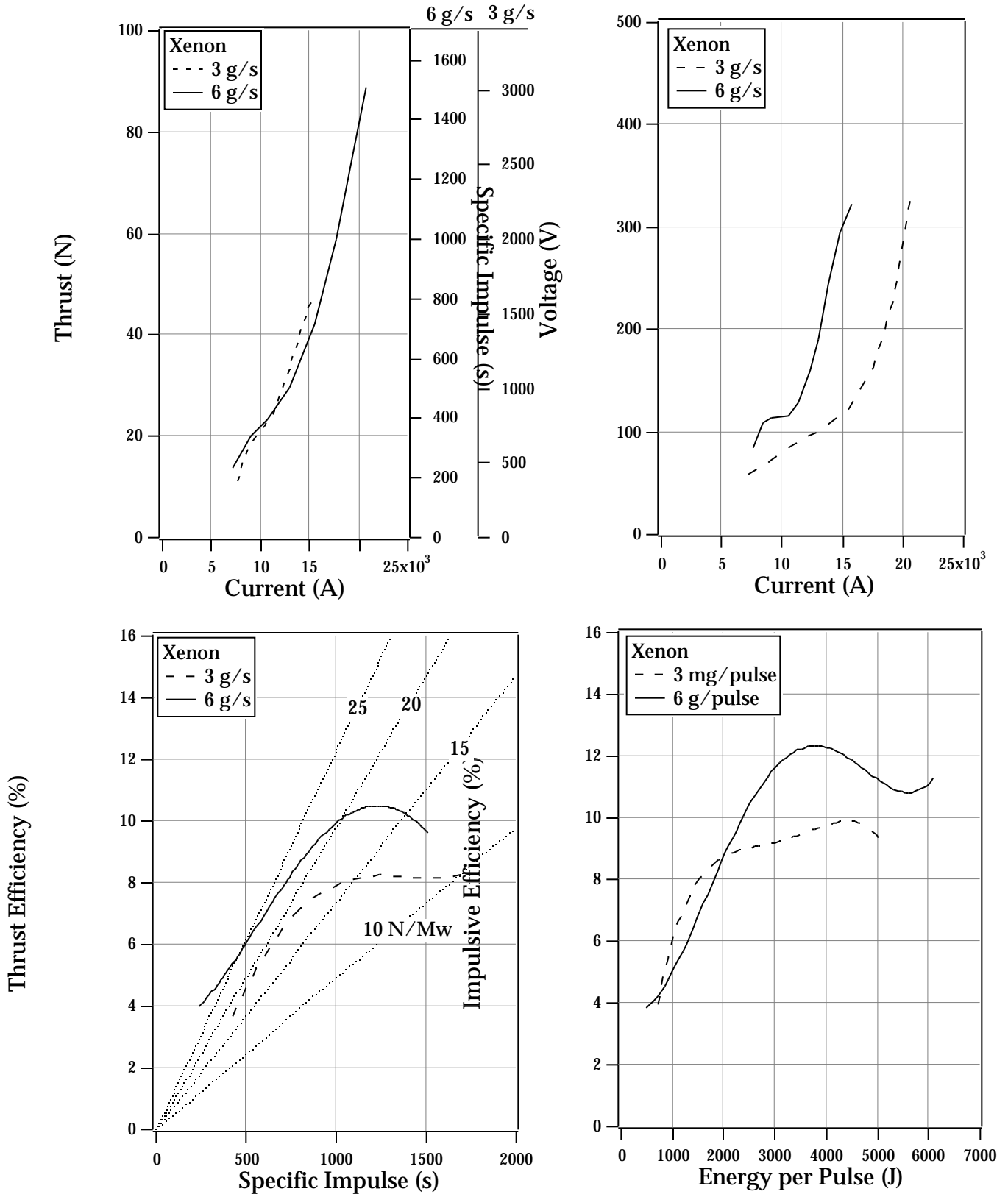


Figure 8: Performance Database for Xenon. The corresponding error bars can be obtained from the scatter plots in the next figure.

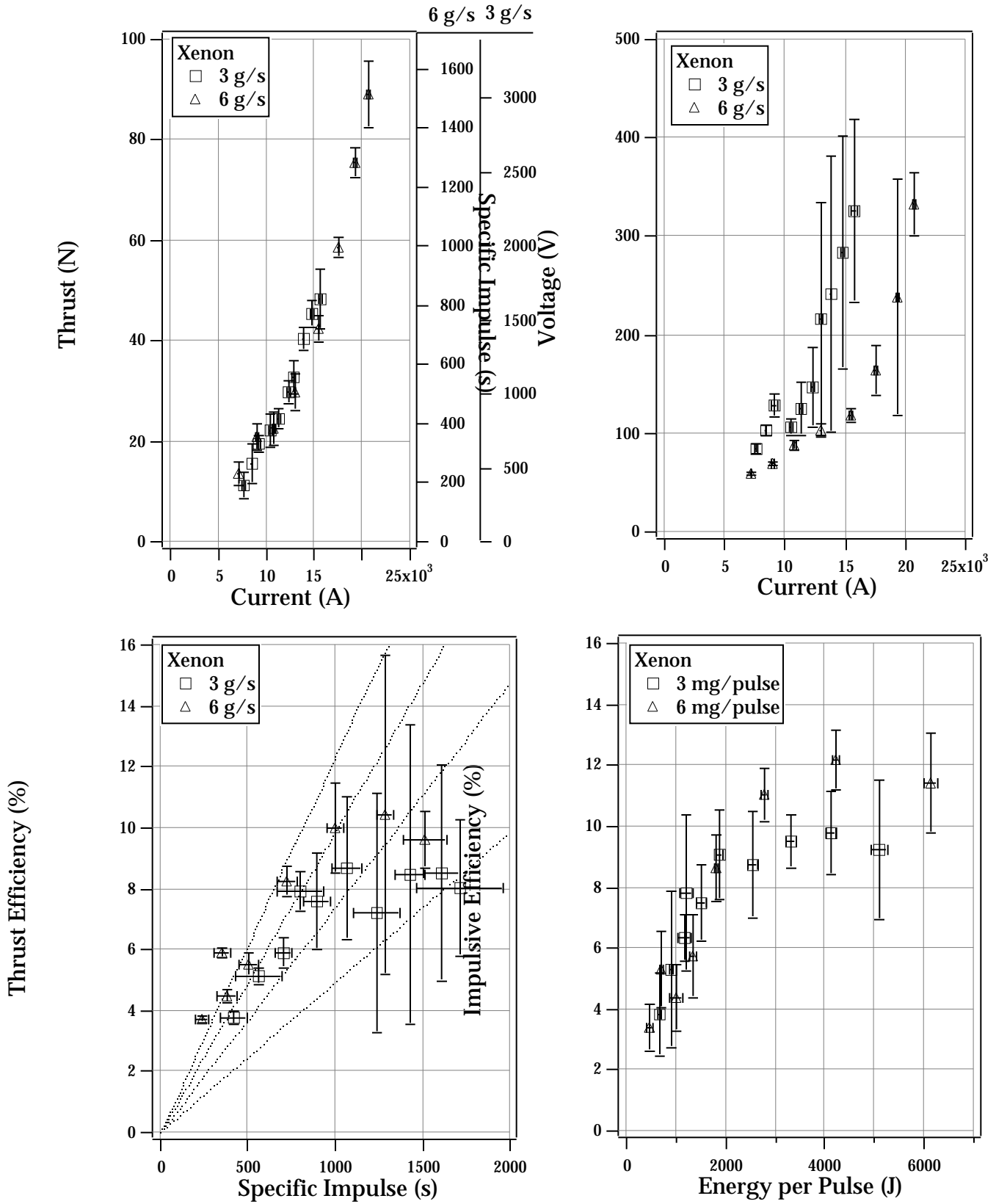


Figure 9: Performance Database for Xenon.

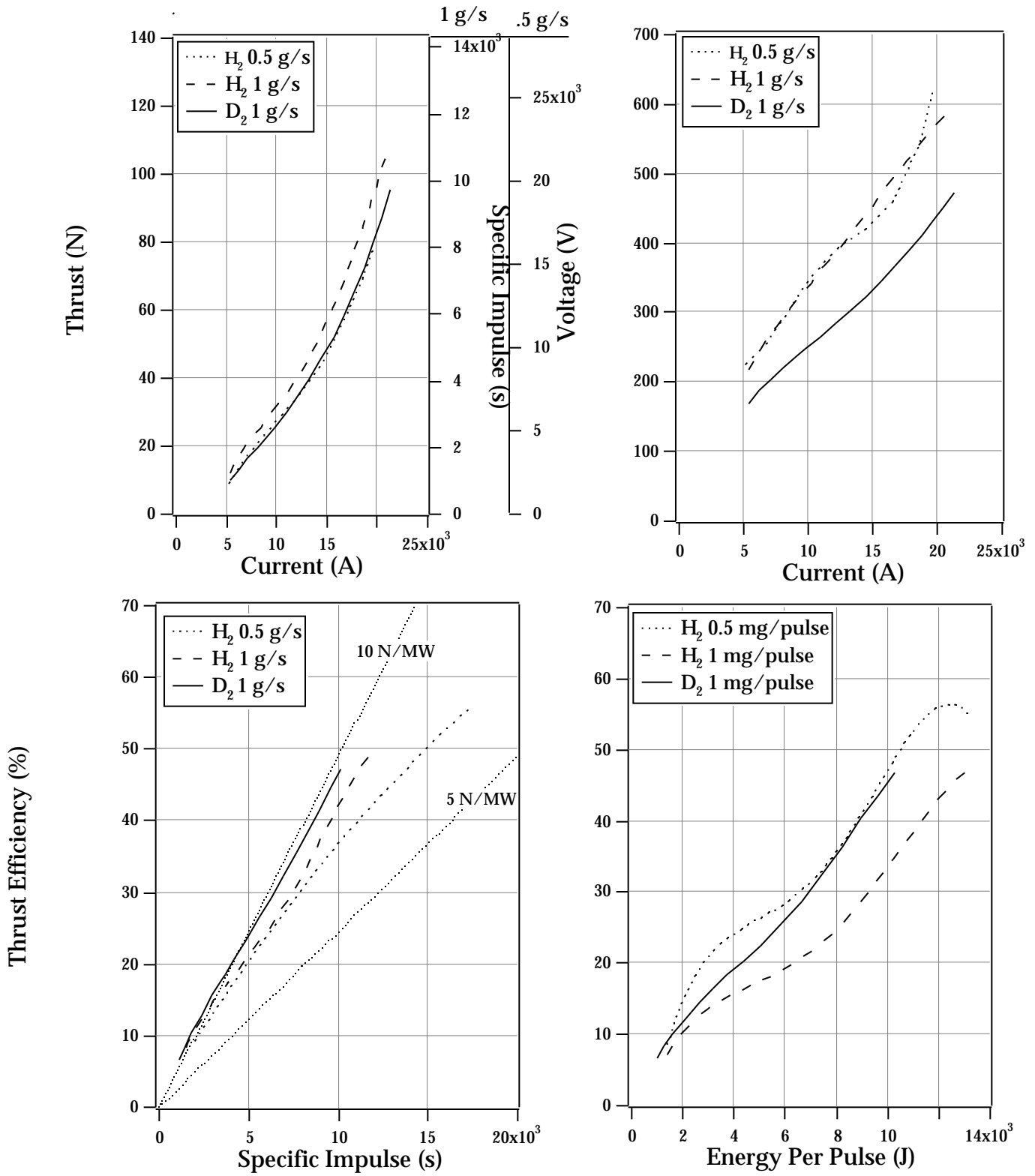


Figure 10: Performance Database for H₂/D₂. The corresponding error bars can be obtained from the scatter plots in the next figure.

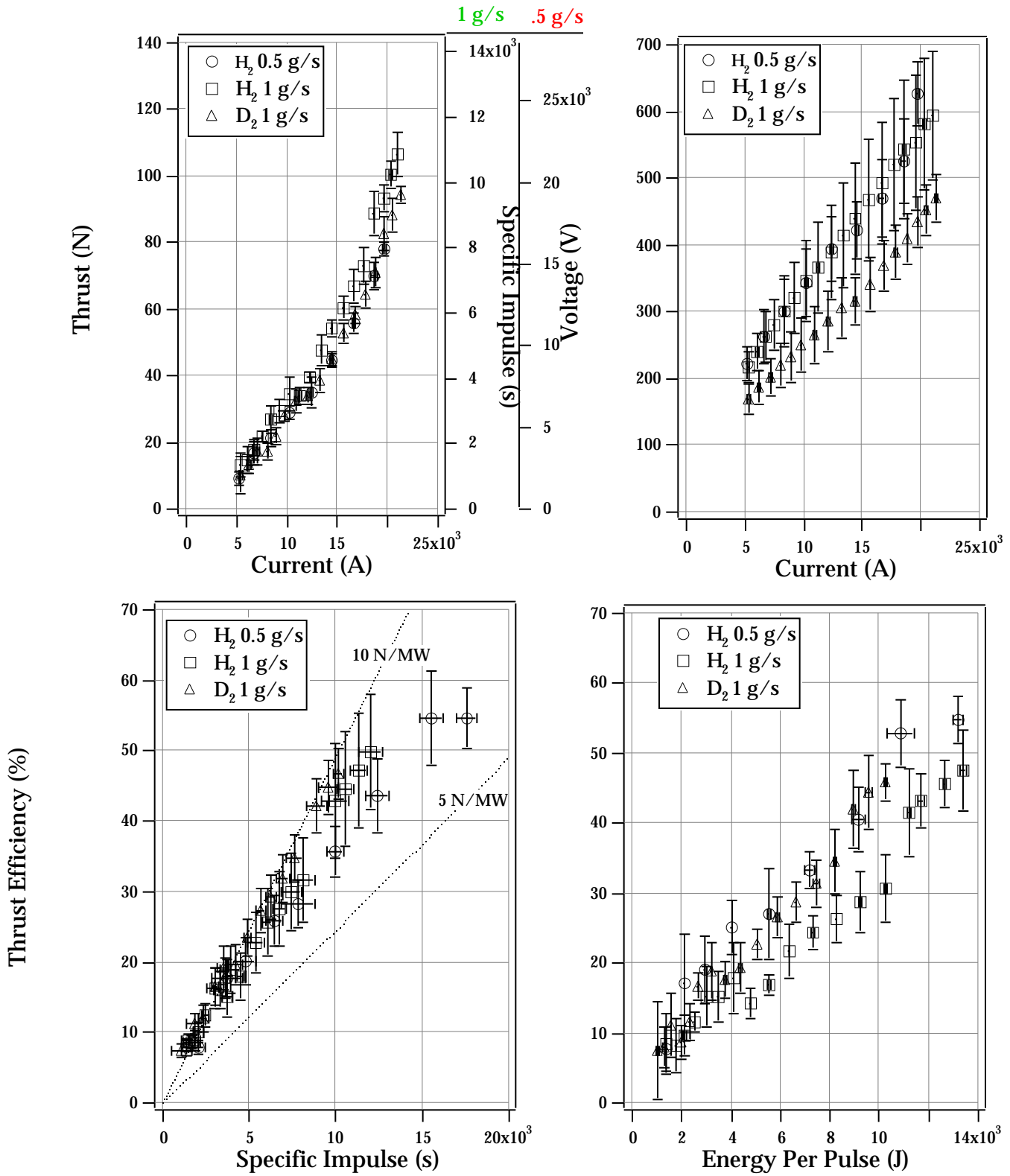


Figure 11: Performance Database for H₂/D₂.